Stability of the puncture method with a generalized BSSN formulation

Helvi Witek[1,2]‡, **David Hilditch**[2]§, **Ulrich Sperhake**[2,3,4,5]‖

[1] Centro Multidisciplinar de Astrofísica — CENTRA, Departamento de Física, Instituto Superior Técnico — IST, Universidade Técnica de Lisboa - UTL, Av. Rovisco Pais 1, 1049-001 Lisboa, Portugal

[2] Theoretisch-Physikalisches Institut, Friedrich-Schiller Universität Jena, Max-Wien Platz 1, 07743 Jena, Germany

[3] Institut de Ciències de l'Espai (CSIC-IEEC), Facultat de Ciències, Campus UAB, E-08193 Bellaterra, Spain

[4] Theoretical Astrophysics 350-17, California Institute of Technology, Pasadena, CA 91125

[5] Department of Physics and Astronomy, The University of Mississippi, University, MS 38677, USA

Abstract. The puncture method for dealing with black holes in the numerical simulation of vacuum spacetimes is remarkably successful when combined with the BSSN formulation of the Einstein equations. We examine a generalized class of formulations modelled along the lines of the Laguna-Shoemaker system and including BSSN as a special case. The formulation is a two parameter generalization of the choice of variables used in standard BSSN evolutions. Numerical stability of the standard finite difference methods is proven for the formulation in the linear regime around flat space, a special case of which is the numerical stability of BSSN. Numerical evolutions are presented and compared with a standard BSSN implementation. We find that a significant portion of the parameter space leads to stable evolutions and that standard BSSN is located near the edge of the stability region. Non-standard parameter choices typically result in smoother behaviour of the evolution variables close to the puncture and thus hold promise for improved accuracy in, e.g., long-term BH binary inspirals, and for overcoming (numerical) stability problems still encountered in some types of black-hole simulations, e.g., in $D \geq 6$ dimensions.

PACS numbers: 04.20.Cv, 04.25.D-, 04.25.dg,

‡ helvi.witek@ist.utl.pt
§ david.hilditch@uni-jena.de
‖ sperhake@tapir.caltech.edu

1. Introduction

Accelerated bodies generate gravitational waves (GWs) in analogy to the emission of electromagnetic waves by accelerated charges. The first direct detection of GWs, expected in the course of the next decade, will not only provide us with the first strong field tests of Einstein's general relativity but also open up an entire new window to the universe. The strongest source of GWs are compact binary systems involving neutron stars and black holes (BHs). Such compact objects have been known for a long time to represent the natural end product of stellar evolution. For instance, stellar-mass BHs are suspected to be the compact members in X-ray binaries [1]. In addition there is now strong observational evidence for the existence of supermassive BHs (SMBHs) at the center of many if not all galaxies [2, 3]. Astrophysical observations in recent decades have thus promoted BHs from the status of a mathematical curiosity to that of a key player in many astrophysical processes.

While GW emission from compact objects has been theoretically predicted for quite a while, the waves' weak interaction makes their direct observation a daunting task, possible only by using modern high precision technology. In particular, there exists now an international network of ground-based laser interferometers (LIGO [4, 5], GEO600 [6, 7], VIRGO [8] and TAMA [9]) operating at or near design sensitivity. A space-borne interferometer called LISA [10] is scheduled for launch in about one decade to supplement such observations with exceptional accuracy in a lower frequency band. Still, the understanding of the radiated wave patterns is crucial for the first detection of GWs as well as for the interpretation of the measured signal. Eventually, the community will be able to gain information about characteristic parameters of the BH system observed via GWs such as the mass ratio and spins.

The modeling of these binary sources of GWs currently employs a variety of techniques. The inspiraling phase of a binary black-hole (BBH) prior to merger as well as the ringdown phase after the merger can be modeled accurately by the approximate post-Newtonian [11] and perturbation methods [12], respectively. In order to simulate the late inspiral and merger of a BBH, however, numerical methods are required to solve the fully non-linear Einstein equations. A numerical treatment requires us to cast the Einstein equations into the form of a time evolution system. This is most commonly done by using the canonical Arnowitt-Deser-Misner "3+1" decomposition [13] as further developed by York [14]; the 4-dimensional spacetime is decomposed into a family of 3-dimensional hypersurfaces labeled by a time coordinate. The geometry of spacetime is determined by the induced 3-metric γ_{ij} on the hypersurfaces and their extrinsic curvature K_{ij}, which describes their embedding. The coordinates are described by the lapse function α and the shift vector β^i. These gauge functions represent the coordinate freedom of general relativity (GR).

For a long time, numerical methods based on this approach faced a variety of problems including the specific formulation of the evolution equations, suitable coordinate choices and the treatment of singularities inherent in the spacetimes. The year 2005 brought about the eventual breakthrough, the first complete simulations of a BBH coalescence [15, 16, 17]. The ensuing years have produced a wealth of results on BBH inspiral pertaining to BH recoil, spin precession and GW data analysis to name but a few (see [18, 19, 20, 21, 22] for recent reviews).

The current generation of successful numerical codes can be divided into two categories. The first class uses the so-called Generalized Harmonic Gauge (GHG) formulation employed in Pretorius' original breakthrough. The second type of codes is commonly referred to as *Moving Puncture* codes, the method underlying the simulations of the Goddard and Brownsville groups. In spite of the remarkable robustness of both methods, it is fair to say that our understanding of why these techniques work so well is limited. The Moving Puncture method in particular has proven robust in even the most demanding simulations of BBHs involving nearly critical spins and velocities close to the speed of light [23, 24, 25, 26]. Previous investigations of this method have concentrated on the structure near the singularity and the impact of gauge conditions [27, 28, 29, 30, 31].

The purpose of the present work is to shed additional light on which ingredients of the Moving Puncture method make this technique so successful. The particular focus of our study is on the underlying formulation of the Einstein equations, the Baumgarte-Shapiro-Shibata-Nakamura (BSSN) formulation [32, 33] as well as a modified version thereof modeled along the lines of the alternative evolution system proposed by Laguna and Shoemaker (LaSh) in 2002 [34]. Such a study is beyond purely academic interest. While the currently employed techniques appear to work well for 3+1 dimensional simulations in the framework of Einstein's general relativity, there is strong motivation to push numerical relativity further. A main target of gravitational wave observations is the testing of GR versus alternative theories of gravity (see [35] for an overview, [36] for solutions of rotating holes in Chern-Simons modified gravity and [37] for hyperbolicity studies of scalar tensor theories of gravity). A further application of numerical relativity, in the context of high energy physics, as motivated by so-called TeV gravity scenarios [38, 39, 40, 41, 42], or by the (conjectured) Anti-de Sitter/Conformal Field theory (AdS/CFT) correspondence [43, 44, 45], will be the simulation of BHs in higher dimensions [46, 47, 48, 49, 50, 51, 52, 53, 54, 55] or non-asymptotically flat spacetimes (see, e.g., [56] for a recent approach).

An improved understanding of the success of the 3+1 GR techniques will be crucial in extending numerical relativity successfully along these lines of future research. From a more practical point of view, alternative schemes might simply be more efficient and result in reduced computational requirements. Unfortunately, we will see further below that the LaSh system does not result in faster simulations.

This paper is structured as follows. The formulation of the LaSh evolution scheme is presented in Sec. 2. In Sec. 3 well-posedness and numerical stability of the LaSh system are studied. The LaSh formulation, implemented as an extension to the Lean code [57], is tested numerically with head-on collision and inspiraling BH binaries. The numerical results are presented in Sec. 4. Finally Sec. 5 contains our conclusions.

2. The LaSh Formulation

2.1. The ADM equations

Both the BSSN and LaSh systems are typically presented as a simultaneous conformal decomposition and readjustment of the ADM equations [33, 58, 59]. For our purposes such a presentation will not suffice. Instead, the addition of definition-differential constraints which alters the characteristic structure of the system and guarantees well-posedness and the conformal decomposition that changes to a convenient form of the evolved variables are considered separately.

In any case one must first introduce the ADM system, which has the evolution part

$$\begin{aligned} \partial_t \gamma_{ij} &= -2\alpha K_{ij} + \mathcal{L}_\beta \gamma_{ij}, && (1)\\ \partial_t K_{ij} &= -D_i D_j \alpha + \alpha[R_{ij} - 2K_{ik}K^k_j + K_{ij}K] + \mathcal{L}_\beta K_{ij}. && (2) \end{aligned}$$

and the physical Hamiltonian and momentum constraints

$$\begin{aligned} H &= R + K^2 - K_{ij}K^{ij} = 0 && (3)\\ M_i &= D_j K_i^j - D_i K = 0\,, && (4) \end{aligned}$$

where

$$R_{ij} = \Gamma^k{}_{ij,k} - \Gamma^k{}_{kj,i} + \Gamma^k{}_{kl}\Gamma^l{}_{ij} - \Gamma^k{}_{il}\Gamma^l{}_{kj}\,. \tag{5}$$

When closed with some gauge choice, the ADM system is typically only weakly hyperbolic and thus does not admit a well-posed Cauchy problem. The BSSN formulation is one of many modifications to the ADM system that can yield a strongly (or even symmetric) hyperbolic problem when coupled to some gauge [60].

2.2. BSSN Constraint addition

Definition-differential constraint: We define the differential constraint

$$G_i \equiv f_i - \gamma^{jk}\Big(\gamma_{ij,k} - \frac{1}{3}\gamma_{jk,i}\Big) = 0\,. \tag{6}$$

Below it will be seen that this choice naturally makes f_i coincide with the relevant BSSN variable.

Constraint addition: The ADM equations are adjusted to

$$\begin{aligned} \partial_t \gamma_{ij} &= \mathrm{ADM}\,, && (7)\\ \partial_t K_{ij} &= \mathrm{ADM} + \alpha G_{(i,j)} - \frac{1}{3}\alpha\gamma_{ij}\left(H + G_k^{;k}\right)\,, && (8)\\ \partial_t f_i &= \partial_t\left(\gamma^{jk}\gamma_{ij,k} - \frac{1}{3}\gamma^{jk}\gamma_{jk,i}\right)_{\mathrm{ADM}} + 2\alpha M_i + \beta^j G_{(i,j)} \\ &\quad + \frac{1}{\gamma}\beta^j \log(\gamma)_{,j} G_i + \beta^j \gamma_{il}(\gamma^{\frac{1}{3}}\gamma^{lm}_{,j})G_m\,. && (9) \end{aligned}$$

The principal part, i.e., highest derivatives of variables added correspond exactly to those added in the NOR formulation (with $a = b = 1$, $c = d = -1/3$ in the notation of [61]). It is for this reason that Gundlach and Martín-García were able to identify the two systems when analyzing the principal part [61]).

2.3. Conformal decomposition and densitization

Conformal variables and algebraic constraints: The LaSh system [34] takes as its evolved variables

$$\tilde{\gamma}_{ij} = \gamma^{-\frac{1}{3}}\gamma_{ij}\,, \qquad \chi = \gamma^{-\frac{1}{3}}\,, \tag{10}$$

$$\tilde{K} = \chi^{-\frac{3}{2}n_K} K\,, \qquad \tilde{A}^i{}_j = \chi^{-\frac{3}{2}n_K}(K^i{}_j - \delta^i{}_j K/3)\,, \tag{11}$$

$$\tilde{\Gamma}^i = \tilde{\gamma}^{jk}\tilde{\Gamma}^i{}_{jk} = -\partial_j\tilde{\gamma}^{ij}\,. \tag{12}$$

The key difference between LaSh and BSSN is that inside LaSh the trace and tracefree parts of the extrinsic curvature are densitized. Notice, that we recover the standard BSSN equations for vanishing densitization parameter. Note that the definition of G_i gives

$$G_i = f_i - \gamma^{jk}\Big(\gamma_{ij,k} - \frac{1}{3}\gamma_{jk,i}\Big) = \tilde{\gamma}_{ij}\tilde{\Gamma}^j - \tilde{\gamma}^{jk}\tilde{\gamma}_{ij,k}. \tag{13}$$

Evolution equations and constraints: Taking a time derivative of the definitions, substituting the evolution equations and rewriting in terms of the evolved variables gives the LaSh equations - up to the algebraic constraints $D = \ln(\det\tilde{\gamma}) = 0$, $S = \tilde{\gamma}_{l[i}\tilde{A}^l{}_{j]} = 0$, $T = \tilde{\gamma}^{ij}\tilde{A}_{ij} = 0$, which are assumed to be satisfied exactly. The unknowns evolve according to

$$\partial_t\tilde{\gamma}_{ij} = -2\alpha\tilde{A}_{ij} + \beta^k\tilde{\gamma}_{ij,k} + 2\tilde{\gamma}_{k(i}\beta^k_{,j)} - \frac{2}{3}\tilde{\gamma}_{ij}\beta^k_{,k},\,, \tag{14}$$

$$\partial_t\chi = \beta^i\chi_{,i} + \frac{2}{3}\chi(\alpha\chi^{\frac{3}{2}n_K}\tilde{K} - \beta^i{}_{,i})\,, \tag{15}$$

$$\begin{aligned}\partial_t\tilde{A}^i{}_j = {} & -\chi^{-3n_K/2}[-D^iD_j\alpha - \alpha R^i{}_j]^{\mathrm{tf}} + (1-n_K)\chi^{3n_K/2}\alpha\tilde{K}\tilde{A}^i{}_j \\ & + \beta^k\partial_k\tilde{A}^i{}_j - \tilde{A}^k{}_j\partial_k\beta^i + \tilde{A}^i{}_k\partial_j\beta^k + n_K\tilde{A}^i{}_j\partial_k\beta^k\,,\end{aligned} \tag{16}$$

$$\begin{aligned}\partial_t\tilde{K} = {} & -\chi^{-\frac{3}{2}n_K}D_iD^i\alpha + \beta^k\partial_k\tilde{K} + n_K\tilde{K}\partial_k\beta^k \\ & + \chi^{3n_K/2}\alpha(\tilde{A}^{ij}\tilde{A}_{ij} + (1-3n_K)\tilde{K}^2/3)\,,\end{aligned} \tag{17}$$

$$\begin{aligned}\partial_t\tilde{\Gamma}^i = {} & -2\tilde{A}^{ij}\alpha_{,j} + 2\alpha(\tilde{\Gamma}^i_{jk}\tilde{A}^{jk} - 2\tilde{A}^{ij}\ln(\chi)_{,j} - \frac{2}{3}\tilde{\gamma}^{ij}(\chi^{3n_K/2}\tilde{K})_{,j}) \\ & + \tilde{\gamma}^{jk}\beta^i_{,jk} + \frac{1}{3}\tilde{\gamma}^{ij}\beta^k_{,kj} + \beta^j\tilde{\Gamma}^i_{,j} - \Big(\tilde{\Gamma}\Big)^j_{\mathrm{d}}\beta^i_{,j} + \frac{2}{3}\Big(\tilde{\Gamma}\Big)^i_{\mathrm{d}}\beta^j_{,j}\,,\end{aligned} \tag{18}$$

where $[\ ]^{\mathrm{tf}}$ denotes the trace free part, $(\ )_{\mathrm{d}}$ denotes the definition of those terms rather than the evolved variable and R_{ij} is partially rewritten in terms of $\tilde{\Gamma}^i$,

$$R_{ij} = R^\chi_{ij} + \tilde{R}_{ij}\,, \tag{19}$$

$$R^\chi_{ij} = \frac{1}{2\chi}\tilde{D}_i\tilde{D}_j\chi + \frac{1}{2\chi}\tilde{\gamma}_{ij}\tilde{D}^l\tilde{D}_l\chi - \frac{1}{4\chi^2}\tilde{D}_i\chi\tilde{D}_j\chi - \frac{3}{4\chi^2}\tilde{\gamma}_{ij}\tilde{D}^l\chi\tilde{D}_l\chi\,, \tag{20}$$

$$\begin{aligned}\tilde{R}_{ij} = {} & -\frac{1}{2}\tilde{\gamma}^{lm}\tilde{\gamma}_{ij,lm} + \tilde{\gamma}_{k(i|}\tilde{\Gamma}^k_{|,j)} + \Big(\tilde{\Gamma}\Big)^k_{\mathrm{d}}\tilde{\Gamma}_{(ij)k} \\ & + \tilde{\gamma}^{lm}\Big(2\tilde{\Gamma}^k_{l(i}\tilde{\Gamma}_{j)km} + \tilde{\Gamma}^k_{im}\tilde{\Gamma}_{klj}\Big)\,.\,,\end{aligned} \tag{21}$$

$\tilde{D}_i$ denotes the covariant derivative compatible with the conformal metric. The physical constraints are rewritten

$$H = R - \chi^{3n_K}(\tilde{A}^j{}_k\tilde{A}^k{}_j - \frac{2}{3}\tilde{K}^2) = 0\,, \tag{22}$$

$$M_i = \tilde{A}^j{}_{i,j} - \frac{2}{3}\tilde{K}_{,i} - \frac{n_K}{\chi}\tilde{K}\chi_{,i} - \tilde{A}^j{}_m\tilde{\Gamma}^m_{ji} - \frac{3}{2\chi}(1-n_K)\tilde{A}^m{}_i\chi_{,m} = 0\,. \tag{23}$$

The differential constraints are given by Eq. 13 and algebraic constraints by

$$S \equiv \tilde{\gamma}_{l[i}\tilde{A}^l{}_{j]} = 0\,, \quad T \equiv \tilde{\gamma}^{ij}\tilde{A}_{ij} = 0\,, \quad D \equiv \ln(\det\tilde{\gamma}) = 0\,. \tag{24}$$

Numerical relativity codes use a technique called constraint projection to enforce the algebraic constraints. When operations are performed which may violate the D, S and T constraints they are enforced explicitly. It is for this reason that we need not worry about the algebraic constraints in the construction of (14-18); the continuum system they represent is identical to that of (7-9). BSSN evolves $\tilde{A}_{ij}$, so does not have the symmetry constraint S.

2.4. Gauge conditions

The successful evolution of binary BH systems has been possible with the now standard 1+log variant of the Bona-Massó slicing condition,

$$\partial_t\alpha = -2\alpha K + \beta^i\partial_i\alpha. \tag{25}$$

Stationary data for this gauge has been studied in [27, 28, 29, 30, 31, 62]. In our numerical evolutions the Γ-driver shift condition

$$\partial_t\beta^i = \mu_S B^i + \xi_1\beta^j\partial_j\beta^i\,, \tag{26}$$

$$\partial_t B^i = \partial_t\tilde{\Gamma}^i - \xi_2\beta^j\partial_j\tilde{\Gamma}^i - \eta B^i + \xi_1\beta^j\partial_j\beta^i\,, \tag{27}$$

is used with $(\mu_S, \xi_1, \xi_2, \eta) = (1, 0, 0, 1)$ unless otherwise stated. We refer to the combination of the 1+log lapse and Γ-driver shift as "puncture gauge". Conditions in which the lapse and shift are promoted to the status of evolved variables are often called *live gauge* conditions. In analytic studies however it is common to consider a fixed, densitized lapse

$$Q = \gamma^{-\frac{n_Q}{2}}\alpha = \chi^{\frac{3n_Q}{2}}\alpha. \tag{28}$$

and fixed shift. In contrast to BSSN the LaSh system takes the densitized lapse Q as a dynamical variable. It is evolved according to the 1+log condition (25) rewritten in terms of Q. The original LaSh system [34] is modified here by the consideration of different densitization parameters n_K and n_Q for the extrinsic curvature and the lapse. When comparing the computational cost of BSSN and LaSh in section 4 we additionally evolve LaSh in the downstairs form of the conformal extrinsic curvature $\tilde{A}_{ij}$. Whereas in [63] the focus was on changing PDE properties of the formulation and holding the variables fixed, here we consider the effect of a change of variables alone.

3. Well-posedness and numerical stability

The well-posedness of the LaSh system with either the puncture gauge or a fixed densitized lapse and shift is guaranteed (assuming that the D,S and T constraints are satisfied) by the results of [61], so verifying these properties for the system linearized around flat space is in its own right uninteresting. However we wish to demonstrate the numerical stability of the LaSh system around flat-space. The approach for the semi-discrete scheme is analogous to that for the continuum system, so we first tackle that problem. In Sec. 3.1 we briefly recap the theoretical background. Next, in Sec. 3.2 we use characteristic variables to demonstrate well-posedness for the continuum system. The analysis is then extended to the semi-discrete case, and follows closely the method of [64, 65]. Finally, we deal with the algebraic constraints in the fully-discrete system by demonstrating that the natural semi-discrete limit of the standard implementation (with constraint projection) is given by the systems considered in Sec 3.2.

3.1. Theoretical background

Continuum system: The linear, constant coefficient, first order in time and second order in space time evolution problem

$$\partial_t u = P[\partial_x]u, \quad u(t=0,x) = f(x) \tag{29}$$

is called well-posed with respect to a norm $||\cdot||$ if for every smooth, periodic $f(x)$ there exists a unique smooth spatially periodic solution and there are constants C, K such that for $t \geq 0$

$$||u(t,\cdot)|| \leq Ke^{Ct}||u(0,\cdot)||. \tag{30}$$

A hermitian matrix $\hat{H}(\omega)$ is called a symmetrizer of the system if the energy $\hat{u}^*\hat{H}\hat{u}$ is conserved by the principal part of the Fourier transformed system, with

$$K^{-1}I_\omega \leq \hat{H} \leq KI_\omega, \quad I_\omega \equiv \begin{pmatrix} \omega^2 & 0 \\ 0 & I \end{pmatrix}, \tag{31}$$

for some $K > 0$ constant, for every frequency ω in Fourier space ($\hat{u}$ denotes the Fourier transformed function.) We say that the Hermitian matrices A, B satisfy the inequality $A \leq B$ if $y^\dagger A y \leq y^\dagger B y$ for every y. Well-posedness is equivalent to the existence of a symmetrizer [66], which is in turn equivalent to the existence of a complete set of characteristic variables.

Discrete system: We introduce a grid

$$\mathbf{x}_j = (x_{j_1}, y_{j_2}, z_{j_3}) = (j_1 h, j_2 h, j_3 h), \tag{32}$$

with $j_i = 0, \ldots N_r - 1$ and $h = \frac{2\pi}{N}$ is the spatial resolution. We denote

$$D_+ v_i = \frac{1}{h}(v_{i+1} - v_i), \quad D_- v_i = \frac{1}{h}(v_i - v_{i-1})\,, \quad D_0 v_i = \frac{1}{2h}(v_{j+1} - v_{j-1})\,. \tag{33}$$

The standard second order accurate discretization is written

$$\partial_i \to D_{0i}\,, \quad \partial_i\partial_j \to D^{(2)}_{ij} = \left\{ \begin{array}{ll} D_{0i}D_{0j} & i \neq j \\ D_{+i}D_{-i} & i = j \end{array} \right. \tag{34}$$

For brevity, we do not consider higher order discretization. Fourier transforming reveals

$$\hat{D}^{(1)}_i = \frac{i}{h} s_i\,, \quad \hat{D}^{(2)}_{ij} = \left\{ \begin{array}{ll} -\frac{1}{h^2} s_i s_j & i \neq j \\ -\frac{4}{h^2} t_i^2 t_j^2 & i = j \end{array} \right. \tag{35}$$

We abbreviate $s_i = \sin\xi_i$ and $t_i = \sin\xi_i/2$, and write

$$\xi_r = \omega_r h = -\pi + \frac{2\pi}{N}, -\pi + \frac{4\pi}{N}, ..., \pi. \tag{36}$$

where $\omega_r = -\frac{N}{2} + 1, ..., \frac{N}{2}$ and $r = 1, 2, 3$. The time step k is related to the spatial resolution h through the Courant factor $k = \lambda_c h$. Finally, we use the notation

$$\omega^2 = -\eta^{ij}\hat{D}_{0i}\hat{D}_{0j}, \qquad \Omega^2 = -\eta^{ij}\hat{D}^{(2)}_{ij}, \tag{37}$$

where η^{ij} is just the identity matrix, so that $\Omega^2 = \sum_{i=1}^3 |\hat{D}_{+i}|^2$. The results for numerical stability with a polynomial method of lines time-integrator are analogous to the result at the continuum: if there exists a hermitian $\hat{H}(\xi)$ for every grid frequency ξ such that the energy $\hat{u}^*\hat{H}\hat{u}$ is conserved by the Fourier-transformed semi-discrete principal system and satisfies

$$K^{-1}I_\Omega \leq \hat{H} \leq K I_\Omega, \quad I_\Omega \equiv \left(\begin{array}{cc} \Omega^2 & 0 \\ 0 & I \end{array} \right), \tag{38}$$

with K as above, then it is possible to construct a discrete symmetrizer for the semi-discrete problem without lower order terms. If the spectral radius of the product of the time-step and the semi-discrete symbol is bounded by a value that depends on the time-integrator, then the system is stable with respect to the norm

$$||u||^2_{h,D_+} \equiv ||u_s||^2_h + ||u_f||^2_h + \sum_{i=1}^{3} ||D_{+i}u_s||^2_h, \tag{39}$$

where the subscript distinguishes between variables that appear as second derivatives in the continuum system. The estimate

$$||u^{n\Delta t}||_{h,D_+} \leq K e^{Cn\Delta t}||u^0||_{h,D_+}, \tag{40}$$

then holds. For details we refer the reader to [64].

Discussion: A straightforward way to construct characteristic variables for the continuum system is to perform a 2+1 decomposition. One then ends up with decoupled scalar, vector and tensor sectors which are hopefully straightforward to diagonalize. Diagonalisability of a system guarantees the existence of a complete set of eigenvectors, which in turn guarantees well-posedness in some norm. For the discrete system, a similar approach is not possible with the standard discretization because the various blocks of the system remain coupled. This complication is caused by the fact that under the standard discretization the second derivative is not equivalent to a repeated application of the first derivative. We will see in the following sections that this forces us to consider significantly larger matrices, and that for the main case of interest, the stability of the LaSh formulation with puncture gauge, the calculation is impractical. One may also consider the numerical stability of systems with the D_0^2 discretization, in which second derivatives are approximated by repeated application of the centered difference operator D_0. In this case it is possible to make a $2+1$ decomposition of the semi-discrete system. Unfortunately, the discretization suffers from the problem that the highest frequency mode on the grid is not captured by the scheme. For the Fourier transformed system this property implies that the transformed spatial derivatives vanish, which typically prevents one from building an estimate on the highest frequency mode. Although artificial dissipation may restore stability, we do not consider the D_0^2 discretization further.

3.2. Continuum system

Fixed densitized lapse and shift: We begin by linearizing the LaSh system around flat-space. Following [66, 64] we Fourier transform in space, and make a pseudo-differential reduction to first order. Spatial derivatives transform according to $\partial_i \to \imath w_i$. The system has a complete set of characteristic variables with characteristic speeds $(0, \pm\omega, \pm\sqrt{n_Q}\omega)$. A conserved quantity for the system may be trivially constructed from the characteristic variables. It is straightforward but tedious to demonstrate that the conserved quantity is equivalent to the norm

$$||u||^2_{\mathrm{fd}} = ||\gamma_{ij}||^2 + ||K_{ij}||^2 + ||f_i||^2 + \sum_{k=1}^{3} ||\gamma_{ij,k}||^2 \tag{41}$$

Puncture gauge: For simplicity we consider the time-integrated Γ-driver shift condition

$$\partial_t \beta_i = f_i. \tag{42}$$

The transformed vector of evolved variables is $\hat{u} = (\hat{\gamma}_{ij}, \hat{\alpha}, \hat{f}_k, \hat{K}_{lm}, \hat{\beta}_n)$. The principal symbol is

$$\hat{P}^\mu{}_\nu = \begin{pmatrix} 0 & 0 & 0 & -2\delta^l_i\delta^m_j & 2\imath w\hat{\omega}_{(i}\delta^n_{j)} \\ 0 & 0 & 0 & -2\eta^{lm} & 0 \\ 0 & 0 & 0 & -\frac{4}{3}\imath\eta^{lm}w\hat{\omega}_k & -w^2\left(\delta^n_k + \frac{1}{3}\hat{\omega}^n\hat{\omega}_k\right) \\ \frac{1}{2}w^2[\delta^i_l\delta^j_m + \frac{1}{3}\eta^{ij}\hat{\omega}_l\hat{\omega}_m]^{\mathrm{tf}} & w^2\hat{\omega}_l\hat{\omega}_m & \imath w[\hat{\omega}_{(l}\delta^k_{m)}]^{\mathrm{tf}} & 0 & 0 \\ 0 & 0 & \delta^k_n & 0 & 0 \end{pmatrix}. \tag{43}$$

We denote $w_i = w\hat{w}_i$, with $w = |w|$. Here “trace-free” denotes that the trace is removed in downstairs indices. The characteristic variables can be constructed from the matrix

$$T^{-1} = \begin{pmatrix} -\frac{1}{3}\imath w\eta^{ij} & -\frac{1}{3}\imath w & \hat{\omega}^k & 0 & 0 \\ 0 & \pm\frac{1}{\sqrt{2}}\imath w & 0 & \eta^{lm} & 0 \\ 0 & -\imath w & \hat{\omega}^k & \pm\sqrt{\frac{2}{3}}\eta^{lm} & \pm\sqrt{\frac{2}{3}}\imath w\hat{\omega}^n \\ 0 & 0 & -\hat{\omega}_{(i}\delta^k_{j)} + \hat{\omega}_i\hat{\omega}_j\hat{\omega}^k & 0 & \pm\imath w[\hat{\omega}_{(i}\delta^n_{j)} - \hat{\omega}_i\hat{\omega}_j\hat{\omega}^n] \\ \frac{1}{2}\imath w[\delta^i_p\delta^j_q + \frac{1}{3}\hat{\omega}_p\hat{\omega}_q\eta^{ij}]^{\mathrm{tf}} & -\frac{8}{3}\imath w[\hat{\omega}_p\hat{\omega}_q]^{\mathrm{tf}} & -[\delta^k_{(p}\hat{\omega}_{q)} - 2\hat{\omega}_p\hat{\omega}_q\hat{\omega}^k]^{\mathrm{tf}} & \pm[\delta^l_p\delta^m_q - \frac{11}{3}\eta^{lm}\hat{\omega}_p\hat{\omega}_q]^{\mathrm{tf}} & \pm 2\imath w[\hat{\omega}_p\hat{\omega}_q]^{\mathrm{tf}}\hat{\omega}^n \end{pmatrix} \tag{44}$$

through $U_c = T^{-1}u$. The characteristic speeds corresponding to each row are $(0, \pm\sqrt{2}w, \pm\sqrt{2/3}w, \pm w, \pm w)$. The conserved quantity is given by

$$\begin{aligned}
&\left(-\frac{4a}{\epsilon_1} + f\left(1 - \frac{1}{\epsilon_3} - \frac{4}{\epsilon_5} - \frac{8}{3\epsilon_7}\right)\right)\frac{w^2}{4}|\hat{\gamma}_{ij}|^2 + \left(\frac{a}{9} + \frac{c}{2} + d\right)w^2|\hat{\alpha}|^2 + ew^2|\hat{\beta}_i|^2 + f|\hat{K}_{ij}|^2 \\
&+ \left(e - a\epsilon_1 - f\left(\epsilon_3 + \epsilon_5 + \frac{2\epsilon_7}{3}\right)\right)|\hat{f}_i|^2 \\
&\leq E_C \leq \qquad\qquad (45) \\
&\left(4a\left(\frac{1}{3} + \frac{1}{\epsilon_2}\right) + f\left(\frac{28}{9} + \frac{1}{\epsilon_4} + \frac{4}{\epsilon_6} + \frac{8}{3\epsilon_8}\right)\right)\frac{w^2}{4}|\hat{\gamma}_{ij}|^2 + \left(\frac{a}{9} + \frac{c}{2} + d + \frac{256}{27}f\right)w^2|\hat{\alpha}|^2 \\
&+ (2d + 4e + 16f)\,w^2|\hat{\beta}_i|^2 + \left(3c + 2d + \frac{436}{9}f\right)|\hat{K}_{ij}|^2 \\
&+ \left(a(3 + \epsilon_2) + 3d + 4e + f\left(14 + \epsilon_4 + \epsilon_6 + \frac{2\epsilon_8}{3}\right)\right)|\hat{f}_i|^2 .
\end{aligned}$$

By choosing $a = \frac{1}{24}$, $c = d = f = 1$, $e = 26$ and $\epsilon_1 = 2$, $\epsilon_2 = \epsilon_4 = \epsilon_6 = \epsilon_8 = 1$, $\epsilon_3 = 4$, $\epsilon_5 = 16$, $\epsilon_7 = 8$ we obtain

$$K^{-1}||\hat{u}||^2_{\text{pg}} \leq E_C \leq K||\hat{u}||^2_{\text{pg}} \qquad (46)$$

where $K = 125$, and have demonstrated that the conserved quantity is equivalent to the norm

$$||\hat{u}||^2_{\text{pg}} = w^2||\hat{\gamma}_{ij}||^2 + w^2||\hat{\alpha}||^2 + w^2||\hat{\beta}_i||^2 + ||\hat{K}_{ij}||^2 + ||\hat{f}_i||^2 . \qquad (47)$$

Parseval's relation implies equivalence with

$$||u||^2_{\text{pg}} = ||\gamma_{ij}||^2 + ||\alpha||^2 + ||\beta_i||^2 + ||K_{ij}||^2 + ||f_i||^2 + \sum_{k=1}^{3}(||\gamma_{ij,k}||^2 + ||\alpha_{,k}||^2 + ||\beta_{i,k}||^2) \qquad (48)$$

in physical space.

3.3. Discrete system

Fixed densitized lapse and shift: We now consider the semi-discrete system with fixed densitized lapse and shift. As in the continuum case we linearize around flat-space. The difference operators transform as described in Sec. 3.1. We consider only the case $n_Q = 1$. We define

$$\hat{\tau} = \eta^{ij}\hat{\gamma}_{ij}, \quad \hat{\Gamma}_i = \hat{f}_i - \frac{2}{3}D_{0i}\hat{\tau}. \qquad (49)$$

Decomposing the system into trace, off-diagonal, and diagonal terms adjusted by the weighting $t_i^4\hat{\gamma}_{ii} = \tilde{\gamma}_{ii}$ and $t_i^4\hat{\Gamma}_i = \tilde{\Gamma}_i$ various sectors of the system decouple. In the following γ_{ij} explicitly means $i \neq j$. The principal symbol is

$$(0) \qquad\qquad \hat{\Gamma}_i, \qquad (50)$$

$$\begin{pmatrix} 0 & -2 \\ \frac{1}{2}\Omega^2 & 0 \end{pmatrix} \qquad \begin{pmatrix} \hat{\tau} \\ \hat{K} \end{pmatrix}, \qquad (51)$$

$$\begin{pmatrix} 0 & 0 & -2 \\ 0 & 0 & 0 \\ \frac{1}{2}\Omega^2 & 1 & 0 \end{pmatrix} \quad \begin{pmatrix} \hat{\gamma}_{ij} \\ \hat{D}_{0(i}\hat{\Gamma}_{j)} \\ \hat{K}_{ij} \end{pmatrix}, \tag{52}$$

$$\begin{pmatrix} 0 & 0 & -2 \\ 0 & 0 & 0 \\ \frac{1}{2}\Omega^2 & 1 & 0 \end{pmatrix} \quad \begin{pmatrix} \tilde{\gamma}^{\mathrm{tf}}_{ii} \\ (\hat{D}_{0i}\tilde{\Gamma}_{i})^{\mathrm{tf}} \\ \tilde{K}^{\mathrm{tf}}_{ii} \end{pmatrix}. \tag{53}$$

The characteristic variables are

$$\hat{\Gamma}_i\,, \quad K \pm \frac{\imath\Omega}{2}\tau\,, \quad K_{ij} \pm \frac{\imath\Omega}{2}\gamma_{ij} \pm \frac{\imath}{\Omega}D_{0(i}\Gamma_{j)}\,, \quad \left(\tilde{K}_{ii} \pm \frac{\imath\Omega}{2}\tilde{\gamma}_{ii} \pm \frac{\imath}{\Omega}D_{0i}\tilde{\Gamma}_i\right)^{\mathrm{tf}} \tag{54}$$

and have speeds $(0, \pm\imath\Omega, \pm\imath\Omega, \pm\imath\Omega)$. The system has a pseudo-discrete reduction to first order that admits a symmetrizer for every grid-frequency. One must treat the lowest frequency separately, but in that case the principal symbol vanishes and so admits the identity as a symmetrizer. By the equivalence of norms in finite dimensional vector spaces we then have numerical stability in the pseudo-discrete norm

$$||\hat{u}||^2_{h,fd} = \Omega^2||\hat{\gamma}_{ij}||^2_h + ||\hat{K}_{ij}||^2_h + ||\hat{f}_i||^2_h + ||\hat{\gamma}_{ij}||^2_h, \tag{55}$$

provided that the von-Neumann condition given by

$$\lambda_C \leq \frac{C_0}{2\chi_2}\,, \tag{56}$$

where $C_0 = 2$ and $C_0 = \sqrt{8}$ for iterated Crank-Nicholson or fourth-order Runge-Kutta and $2\chi_2 = \Omega h$, is satisfied. Parseval's relation guarantees equivalence with the discrete norm

$$||u||^2_{h,D_+,fd} = ||\gamma_{ij}||^2_h + ||K_{ij}||^2_h + ||f_i||^2_h + \sum_{k=1}^{3} ||D_{+k}\gamma_{ij}||^2_h \tag{57}$$

in physical space.

Puncture gauge: The principal symbol is a 19x19 matrix which contains several parameters. We are able to compute characteristic speeds for the system, but they are complicated, so we do not display them here. The lowest freqency mode is again trivial to analyze. In that case the pseudo-discrete reduction to first order has a vanishing principal symbol, and thus admits the identity as a symmetrizer. For the non-maximal modes the principal symbol is complicated. As previously stated, performing a $2+1$ decomposition on the semi-discrete symbol is not helpful, since the various sectors of the system remain coupled. We were therefore unable to find the eigenvectors of the matrix. We considered various subsectors of the full system. Since the (α,K) subsector is exactly the second order in space wave equation, it is trivial to demonstrate numerical stability. We considered also the subsector (f_i,β_j) with the other variables frozen, and find characteristic speeds and variables. Once the two blocks are coupled to give the (α,f_i,K,β_j) subsector, we did not manage to compute eigenvectors in finite time. It is possible to find a complete set of characteristic variables for the highest frequency grid-mode, since the principal symbol in that case takes a simpler form. In Sec. 4 we present robust stability tests of the numerical implementation, which provide evidence that the system is formally numerically stable.

Puncture gauge with non-standard spatial discretization: We are able to find a complete set of characteristic variables for a slightly altered spatial discretization. If one insists on using the D_0^2 operator for the divergence terms $\partial_i\partial_j\beta^j$ in the evolution of f_i the principal symbol becomes, with $\hat{u} = (\hat{\gamma}_{ij}, \hat{\alpha}, \hat{f}_k, \hat{K}_{lm}, \hat{\beta}_n)$,

$$\hat{P}^{\mu}_{\nu} = \begin{pmatrix} 0 & 0 & 0 & -2\delta^l_i\delta^m_j & 2\hat{D}_{(0i}\delta^n_{j)} \\ 0 & 0 & 0 & -2\eta^{lm} & 0 \\ 0 & 0 & 0 & -\frac{4}{3}\eta^{lm}\hat{D}_{0k} & -\Omega^2\delta^n_k + \frac{1}{3}\hat{D}^n_0\hat{D}_{0k} \\ \frac{1}{2}[\Omega^2\delta^i_l\delta^j_m - \frac{1}{3}\eta^{ij}\hat{D}^{(2)}_{lm}]^{\rm tf} & -\hat{D}^{(2)}_{lm} & [\hat{D}_{0(l}\delta^k_{m)}]^{\rm tf} & 0 & 0 \\ 0 & 0 & \delta^k_n & 0 & 0 \end{pmatrix}. \tag{58}$$

As before, one has to consider the lowest and highest frequency grid modes seperately, because in those cases the principal symbol of the system takes a different form. For the lowest frequency mode the principal symbol of the pseudo-discrete reduction to first order again vanishes, and can be dealt with as before. For the sub-maximal frequencies the characteristic variables can be constructed and have characteristic speeds $(0, \pm\imath\sqrt{2}\Omega, \pm\imath\sqrt{(3\Omega^2+\omega^2)/3}, \pm\imath\Omega, \pm\imath\Omega)$. The 0-speed characteristic variable is

$$U_0 = \hat{D}_{0i}\hat{f}^i + \frac{1}{2}(\omega^2 - \Omega^2)\hat{\alpha} + \frac{1}{6}(3\Omega^2 + \omega^2)\tau. \tag{59}$$

The lapse characteristic variable is

$$U_{\pm\sqrt{2}} = \sqrt{2}\hat{K} \pm \imath\Omega\hat{\alpha}, \tag{60}$$

The longitudinal shift characteristic variable is

$$U_{\pm 2/\sqrt{3}} = \imath\hat{D}_{0i}\beta^i - \frac{4\imath}{\omega^2 - \Omega^2}\hat{K} \pm \frac{\sqrt{3}}{3\Omega^2 + \omega^2}\hat{D}_{0i}f^i \mp \frac{4\sqrt{3}}{\sqrt{3\Omega^2 + \omega^2}(\omega^2 - 3\Omega^2)}\hat{\alpha}, \tag{61}$$

and the transverse shift modes are

$$U_{i\pm 1} = \Omega(\hat{D}_{0i}\hat{D}^k_0 + \omega^2\delta^k{}_i)\beta_k \pm (\hat{D}_{0i}\hat{D}^k_0 + \omega^2\delta^k{}_i)f_k. \tag{62}$$

To see that there are only two characteristic variables here one must contract with the vector s_i. Finally the remaining characteristic variables are

$$\begin{aligned} U_{ij\pm 1} = {} & [\hat{D}^{(2)}_{ij} + \omega^2\hat{D}_{0(i}\delta^k_{j)}]^{\rm tf}\hat{\beta}_k \mp \frac{\imath}{\Omega}[\hat{D}^{(2)}_{ij}\hat{D}^k_0]^{\rm tf}\hat{f}_k + \omega^2[\delta^k{}_{(i}\delta^l{}_{j)} + \eta^{kl}\hat{D}^{(2)}_{ij}]\hat{K}_{kl} \\ & \pm \frac{1}{2}\imath\omega^2\Omega[\delta^l{}_{(i}\delta^m{}_{j)} - \frac{1}{3\Omega^2}\eta^{lm}\hat{D}^{(2)}_{ij}]^{\rm tf}\hat{\gamma}_{lm}\,, \end{aligned} \tag{63}$$

where $[\ ]^{\rm tf}$ denotes that the object is trace-free in downstairs indices. For the highest frequency mode the D_0 operator in the principal symbol vanishes. However, the symbol still has a complete set of characteristic variables. The conserved quantity may then be constructed as before with a sum over the grid-modes. The conserved quantity is obviously a norm since it contains every grid-mode, and is therefore equivalent to the standard

$$||u||^2_{h,D_+,\mathrm{pg}} = ||\gamma_{ij}||^2_h + ||\alpha||^2_h + ||\beta_i||^2_h + ||K_{ij}||^2_h + ||f_i||^2_h \\ + \sum_{k=1}^{3}(||D_{+k}\gamma_{ij}||^2_h + ||D_{+k}\alpha||^2_h + ||D_{+k}\beta_i||^2_h) \tag{64}$$

in physical space.

As the calculation does not rely in any significant way on the flat background, it should be simple to extend to the case in which one linearizes around an arbitrary, constant in space background. It may then be possible to extend to the case with variable coefficients in space following [66]. We also anticipate no problems in extending the calculation to higher order finite difference (FD) approximations. In our numerical tests in Sec. 4 we do not perform evolutions with this discretization.

3.4. The algebraic constraints

In this section we demonstrate that the numerical stability of standard numerical implementation of the linearized LaSh (and BSSN) systems, which includes the conformal decomposition of the evolved variables, depends only upon the analysis of the previous section. In order to do so, we show that there is a one-one correspondence between solutions of the original and decomposed systems.

In the linear regime the conformal decomposition is simply a linear combination of the undecomposed variables subject to linear constraints. Consider the semi-discrete system under such a decomposition. Start by defining the decomposed state vector on time slice by $v = Tu$. Here and in what follows we suppress spatial indices. Assume that u has m elements. Then T is an $l \times m$ matrix, v has l elements. We denote the pseudo-inverse of T by S, a matrix which maps from the image of T in $\mathbf{R}^l$ back to $\mathbf{R}^m$ such that

$$ST = I_m. \tag{65}$$

If the evolution equations for u are given by Pu and those for the decomposed variables are $\bar{P}v$ then the two are related as $\bar{P} = TPS$. Denote by $\perp$ the projection operator which maps to the m dimensional hypersurface in $\mathbf{R}^l$ on which the algebraic constraints are satisfied. The algebraic constraints are

$$C = v - \perp v. \tag{66}$$

Consider first the semi-discrete system. Suppose that at a given time the constraints are satisfied. Then we find

$$\partial_t C = \bar{P}v - \perp \bar{P}v = TPu - \perp TPu = 0, \tag{67}$$

where the last equality holds because directly after the application of T the algebraic constraints are satisfied, and therefore the projection operator does nothing. Therefore in the semi-discrete system if the constraints are satisfied initially they remain so, and there is a one-one correspondence between solutions of the decomposed and undecomposed systems.

For the fully discrete system we take an explicit polynomial time-integrator Q for the undecomposed variables and the modified time integrator $\perp Q$ for the decomposed system. Now consider the difference between constraint satisfying data u^n and $v^n = Tu^n$ integrated with the two methods. For brevity we subsume the timestep Δt into P and $\bar{P}$. One finds that

$$\begin{aligned} v^{n+1} - Tu^{n+1} &= \perp Q[\bar{P}][v^n] - TQ[P][u^n] \\ &= \perp Q[TPS][Tu^n] - TQ[P][u^n] \\ &= \perp TQ[P][u^n] - TQ[P][u^n] \\ &= TQ[P][u^n] - TQ[P][u^n] = 0, \end{aligned} \tag{68}$$

where we have used linearity of the system, polynomiality of the time-integrator and the fact that directly after the application of T the algebraic constraints are automatically satisfied, so the projection operator does nothing. Thus the two integration methods are equivalent as desired. Note that in these calculations the modified time integrator $\perp Q$ could be replaced by Q since the unprojected time-step introduces no constraint violation. We have verified these calculations by explicitly comparing evolutions of the linearized conformal LaSh system with and without constraint projection. We prefer to discuss the natural linearization of the non-linear method, which includes the projection. In the non-linear case the unprojected timestep can introduce algebraic constraint violations.

4. Numerical Experiments

The LaSh system is implemented inside the Lean code [57] which is based on the Cactus computational toolkit [67] and the mesh refinement package Carpet [68, 69]. Initial data is constructed by solving the constraint equations with the TwoPunctures spectral solver provided by [70].

We perform the following set of numerical evolutions:

Robust stability tests We perform a subset of the so-called apples with apples tests [71] to demonstrate numerically that the evolution system is formally stable with various choices of the densitization parameters;

Puncture stability We evolve a single BH with different choices of the densitization parameters to establish what restriction is placed on them by insisting on *long-term* stable puncture simulations;

Head-on collisions We compare BSSN evolutions of the head on collision of two BHs with those performed with LaSh. We focus on consistency of the extracted physics at finite resolution;

Binary black hole inspiral We compare BSSN evolutions of inspiraling BHs (Goddard R1 [72]) with those performed with LaSh. We consider the computational

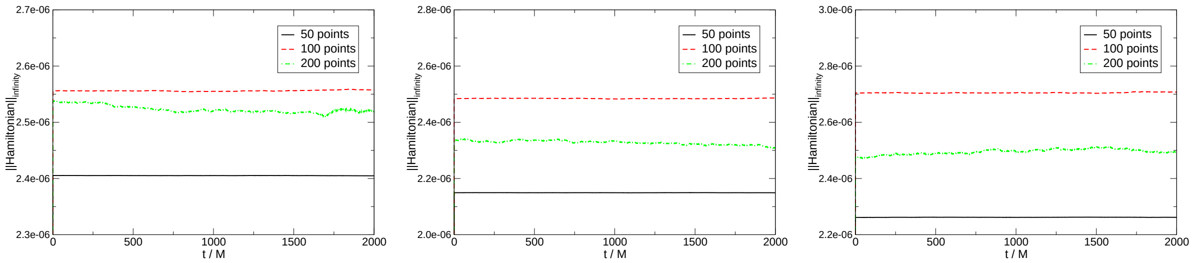

Figure 1. (Color online) Apples with apples stability test using a low (50 grid points, black solid lines), medium (100 grid points, red dashed lines) and high (200 grid points, green dashed-dotted lines) resolution. The tests were performed with the densitization parameters $(n_Q, n_K) = \{(0,0), (0.5,-0.5), (-0.5,0.5)\}$ from left to right, respectively.

costs of simulations with the two systems as well as consistency of the results.

4.1. Robust stability

In Sec. 3.3 we did not succeed in demonstrating numerical stability of the LaSh system with the puncture gauge using standard discretization. We therefore perform robust stability tests following the method in Ref. [71]. The numerical domain is given by $-0.5 < x < 0.5$, $-0.06/\Delta < y < 0.06/\Delta$ and $-0.06/\Delta < z < 0.06/\Delta$ with periodic boundary conditions. We use three different resolutions $h = 0.02/\Delta$, where $\Delta_c = 1$, $\Delta_m = 2$ and $\Delta_f = 4$. The expansion in the y- and z- direction incorporates the three grid points required for fourth order FD stencils. The initial data are given by small perturbations of the Minkowski spacetime

$$\gamma_{ij} = \eta_{ij} + \epsilon_{ij} \, . \tag{69}$$

The ϵ_{ij} are independent random numbers in the range $(-10^{-10}/\Delta, 10^{-10}/\Delta)$, so that terms of the order $\mathcal{O}(\epsilon^2)$ are below round-off accuracy. This means that the evolution remains in the linear regime unless instabilities occur.

We monitor the performance of each simulation by calculating the maximum norm of the Hamiltonian constraint as a function of time. For this study we focus on three choices of the densitization parameters $(n_Q, n_K) = \{(0,0), (0.5,-0.5), (-0.5,0.5)\}$. The results of the robust stability test are plotted in Fig. 1. For all choices of (n_Q, n_K), including the BSSN scaling $(0,0)$, we obtain stable evolutions.

4.2. Puncture stability

We next perform evolutions of a single puncture, studying a wide range of non-trivial densitization parameters. The hyperbolicity analysis of the continuum LaSh scheme presented in Sec. 3.3 is not affected by the choice of densitization parameters provided that the algebraic constraints are enforced. In the previous section we have seen that various choices of the densitization parameters yield evolution systems that are numerically stable. Here we demonstrate that those parameters must be chosen more carefully in order to achieve long-term evolutions of puncture data. We evolve a single, non-rotating BH until $t = 500M$. The BH is initially given by two punctures with mass parameter $m_{1,2} = 0.5M$ located at $z = \pm 10^{-5}M$. Using the notation of Sec. II E of Ref. [57], the grid setup is given in units of M by

$$\{(96, 48, 24, 12, 6, 2, 1, 0.5), 1/32\}\,. \tag{70}$$

We vary both n_Q and n_K in the interval $[-1, 1]$ in steps of $\Delta n = 0.1$. The lifetimes T_l of the simulations are determined as functions of the densitization parameters. The first occurrence of "nans" in the right-hand side of the densitized lapse Q is used as a measure of the lifetime whenever the simulations did not survive for the entire evolution. In Fig. 2 we show the results of this parameter study as a contour plot. In particular, a single puncture can be evolved for at least $t = 500\ M$ using the LaSh system with parameters indicated by the light blue area in the figure. Negative values of the lapse densitization parameter $n_Q < -0.3$ combined with positive values of the curvature densitization parameter $n_K > 0$ let the simulations crash after a short time. In contrast, long term stable evolutions are obtained for the parameter range $n_Q \in [-0.3, 0.9]$, $n_K \in [-1, 0]$, including the BSSN scaling $n_Q = n_K = 0$.

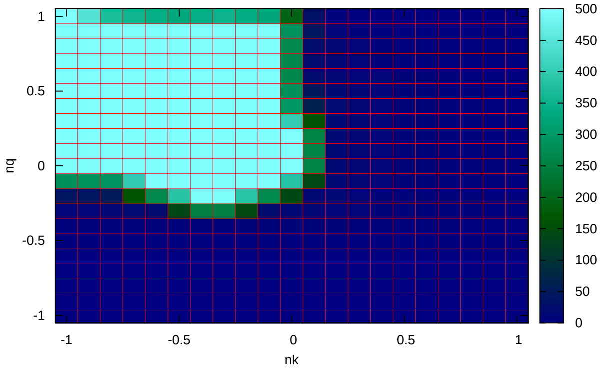

Figure 2. (Color online) Contourplot of the lifetime T_l as function of the densitization parameter n_Q and n_K. Areas colored in dark blue indicate a short lifetime whereas light blue coloring stands for a lifetime of at least $T_l = 500M$.

We can partially understand this behaviour by considering single puncture initial data and their influence on the evolution equations (14-18). On the initial slice the densitized lapse Q is given by

$$Q_0 = \chi^{\frac{3n_Q}{2}}\alpha_0 = \chi^{\frac{3}{2}(n_Q+1/3)}, \tag{71}$$

corresponding to a *pre collapsed* lapse α. Since χ vanishes at the puncture we require $n_Q > -\frac{1}{3}$ to obtain a regular densitized lapse Q_0 on the initial timeslice, in agreement

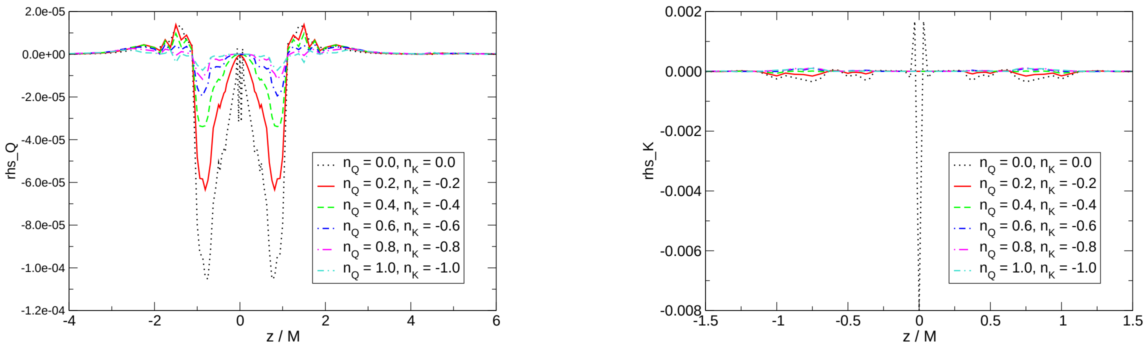

Figure 3. (Color online) Right hand sides of the densitized lapse Q (left panel) and of the trace of the extrinsic curvature $\tilde{K}$ (right panel) after an evolution time of $t = 100M$. We take parameter pairs $(n_Q, n_K) = \{(0,0), (0.2,-0.2), (0.4,-0.4), (0.6,-0.6), (0.8,-0.8), (1,-1)\}$.

with the findings of our parameter study; simulations with $n_Q < -0.3$ crash immediately. Next consider the evolution equations on the initial timeslice. For our initial data they reduce to

$$\partial_t \tilde{\gamma}_{ij} = 0, \qquad \partial_t \chi = 0\,, \tag{72}$$

$$\partial_t \tilde{A}^i{}_j = \chi^{-3n_K/2}[D^i D_j \alpha + \alpha R^i{}_j]^{TF}\,, \tag{73}$$

$$\partial_t \tilde{K} = -\,\chi^{-3n_K/2} D^i D_i \alpha\,, \tag{74}$$

$$\partial_t \tilde{\Gamma}^i = 0\,. \tag{75}$$

Insisting on initially regular evolved variables at the puncture, Eqs. (72-75) require $n_K \leq 0$, also in agreement with our study; numerical experiments violating this condition immediately fail.

For further illustration we plot in Fig. 3 the time derivatives of the densitized lapse Q and the trace of the extrinsic curvature $\tilde{K}$ after an evolution time of $t = 100\ M$. As we simoultaneously increase n_Q and decrease n_K, we obtain smoother profiles. Note that the BSSN case $n_Q = 0 = n_K$ produces the steepest gradients in this comparison. A systematic study of the exceptionally benign behaviour of a non-trivial densitization on the accuracy of 10-15 orbit simulations, especially of spinning, precessing binaries, is beyond the scope of this paper. Our results may, however, point at fertile ground for future research of the LaSh system.

4.3. Head-On Collisions

In this section we study in depth the stability properties of numerical simulations of equal-mass head-on collisions performed with the LaSh system. For this purpose we evolve model $BL2$ of Table II in [57], i.e. two non-spinning holes of with irreducible mass $M_{\mathrm{irr},i} = 0.5\ M$ starting from rest at $z_{1,2} = \pm 5.12\ M$. The computational grid

Run	Grid Setup	d/M	n_Q	n_K	$10^4 E_{rad}/M$
$HD1_c$	$\{(256,128,72,32,16)\times(4,2,1),\ h=1/40\}$	10.24	0.0	0.0	5.51
$HD1_m$	$\{(256,128,72,32,16)\times(4,2,1),\ h=1/44\}$	10.24	0.0	0.0	5.52
$HD1_f$	$\{(256,128,72,32,16)\times(4,2,1),\ h=1/48\}$	10.24	0.0	0.0	5.53
$HD2$	$\{(256,128,72,32,16)\times(4,2,1),\ h=1/48\}$	10.24	0.2	-0.2	5.53
$HD3_c$	$\{(256,128,72,32,16)\times(4,2,1),\ h=1/40\}$	10.24	0.4	-0.4	5.51
$HD3_m$	$\{(256,128,72,32,16)\times(4,2,1),\ h=1/44\}$	10.24	0.4	-0.4	5.52
$HD3_f$	$\{(256,128,72,32,16)\times(4,2,1),\ h=1/48\}$	10.24	0.4	-0.4	5.53
$HD4$	$\{(256,128,72,32,16)\times(4,2,1),\ h=1/48\}$	10.24	0.6	-0.6	5.53

Table 1. Grid structure and physical initial parameters of the simulations of a head-on collsion of an equal mass BH binary. The grid setup is given in terms of the radii of the individual refinement levels as well as the resolution near the punctures h (see Sec. II E in [57] for details). The table further shows the initial coordinate separation d/M of the two punctures. E_{rad}/M is the fraction of the total BH mass that is radiated as gravitational waves. All parameters are given in units of the total BH mass $M = M_1 + M_2$.

consists of a set of nested refinement levels given in units of M by

$$\{(256,128,72,32,16)\times(4,2,1),\ h\}\,, \tag{76}$$

where we have usually chosen $h = M/48$, unless denoted otherwise. We consider the densitization parameters $(n_Q, n_K) = \{(0,0),(0.2,-0.2),(0.4,-0.4),(0.6,-0.6)\}$, denoted as models $HD1$ - $HD4$ in Table 1. For models $HD1$ - $HD3$ we have chosen the Γ-driver shift conditions 27 with $(\mu_S,\xi_1,\xi_2,\eta) = (1,0,0,1)$, whereas in case of model $HD4$ the Γ-driver shift conditions 27 have been taken with $(\mu_s,\xi_1,\xi_2,\eta) = (3/4,1,1,1)$ [73]. Information about gravitational waves emitted during the plunge has been obtained by the Newman-Penrose scalar Ψ_4. In Fig. 4 we present the real part of the dominant mode Ψ_{20}, rescaled by the extraction radius $r_{ex} = 60M$, for models $HD1$-$HD4$. Note, that the imaginary part of Ψ_4 vanishes due to symmetry. We find that the waveforms generated by the different models agree well. We study the convergence of models $HD1$ and $HD3$ by using three different resolutions $h_c = M/40$, $h_m = M/44$ and $h_f = M/48$ referred to as *coarse*, *medium* and *high* resolution. The differences of the $\ell = 2$, $m = 0$ mode of the resulting gravitational radiation are displayed in Fig. 5 and demonstrate overall fourth order convergence for both models. We estimate the discretization error at high resolution in the waveforms Ψ_{20} to be 0.4%, similar to the error reported in [57] for the corresponding BSSN evolutions.

The amount of energy that is radiated throughout the head-on collision computed from, e.g., Eq. (22) in Ref. [56] (see also [19]) is $E_{rad}/M = 0.0553\%$ for models $HD1_f$, $HD2$, $HD3_f$ and $HD4$, again in excellent agreement with Ref. [57]. We estimate the discretization error in the radiated energy to be 0.4% and the error due to finite extraction radius to be 1.6%.

As for single BH evolutions, we observe smoother time derivatives of Q and $\tilde{K}$ for non-vanishing choices of n_Q and n_K. We illustrate this behaviour in Fig. 6 which

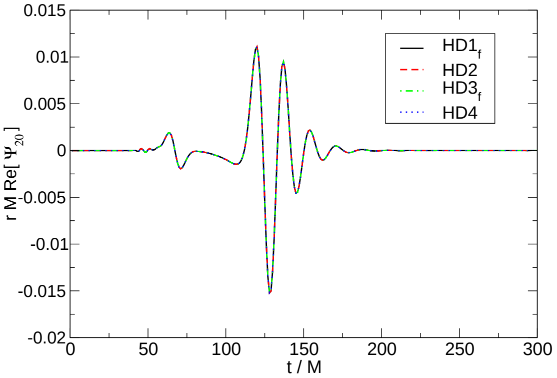

Figure 4. (Color online) Real part of $r_{\rm ex} M \Psi_{20}$, the dimensionless Newman-Penrose scalar, where $r_{ex} = 60M$, for model $HD1_f$ (black solid line), $HD2$ (red dashed line), $HD3_f$ (green dashed-dotted line) and $HD4$ (blue dotted line).

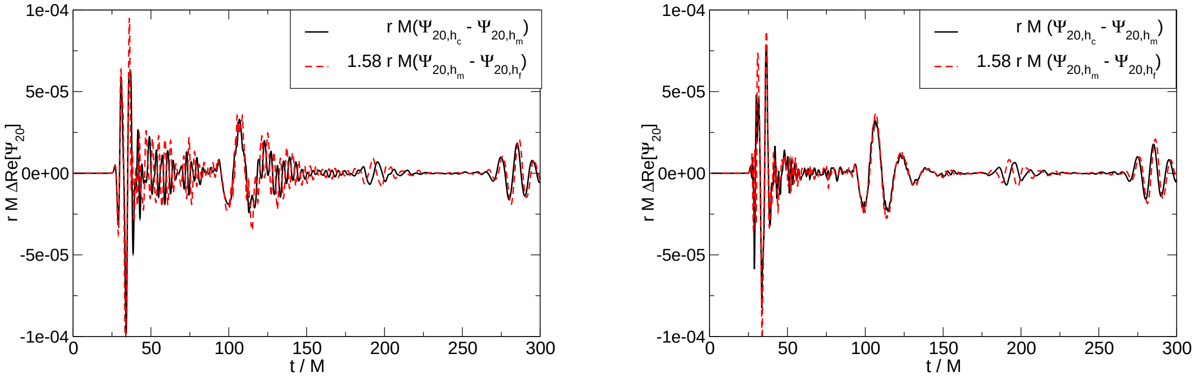

Figure 5. (Color online) Convergence analysis of the real part of Ψ_{20} of the Newman Penrose scalar Ψ_4, re-scaled by the extraction radius $r_{ex} = 40M$, for models $HD1$ (left panel) and $HD3$ (right panel) in Table 1. We show the difference between the low and medium resolution (black solid line) and the medium and high resolution (red dashed line). The latter has been amplified by a factor of $Q = 1.58$ expected for fourth order convergence

shows the time derivatives along the z axis obtained for different values of n_Q and n_K at $t = 10\ M$.

4.4. Inspiraling Black-Holes

In this section we will demonstrate how BBHs can be evolved successfully using the LaSh formulation of the 3+1 Einstein equation in combination with the moving puncture approach. For this purpose we consider the initial configuration labeled R1 in Table I of

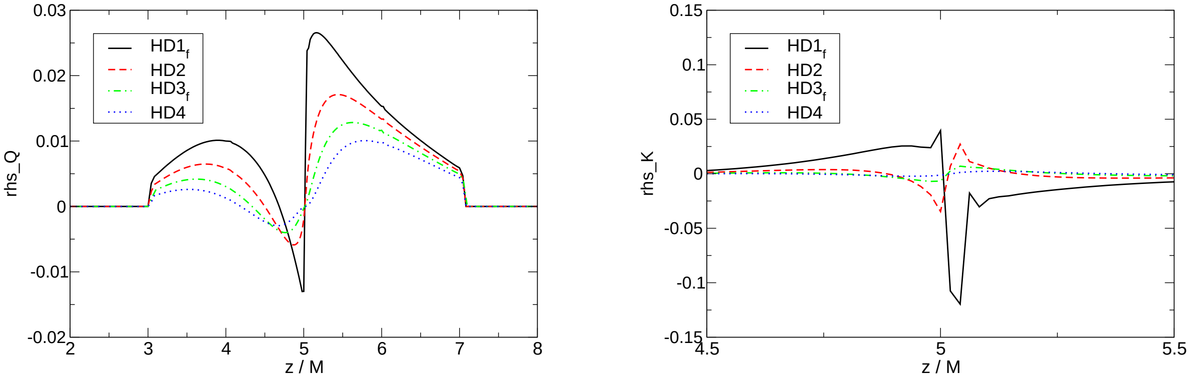

Figure 6. Right hand sides of the densitized lapse Q (left panel) and of the trace of the extrinsic curvature $\tilde{K}$ (right panel) after an evolution time of $t = 10M$ for models $HD1_f$ (solid line), $HD2$ (dashed line), $HD3_f$ (dashed-dotted line) and $HD4$ (dotted line).

Run	ES	Grid Setup	n_Q	n_K	$10^2 E_{rad}/M$
$BSSN$	BSSN	$\{(256, 128, 64, 24, 12, 6) \times (1.5, 0.75),\ 1/48\}$	-	-	-
$LaSh_0$	LaSh	$\{(256, 128, 64, 24, 12, 6) \times (1.5, 0.75),\ 1/48\}$	0.4	-0.4	-
$LaSh_c$	LaSh	$\{(256, 128, 64, 24, 12, 6) \times (1.5, 0.75),\ 1/52\}$	0.4	-0.4	3.69
$LaSh_m$	LaSh	$\{(256, 128, 64, 24, 12, 6) \times (1.5, 0.75),\ 1/56\}$	0.4	-0.4	3.68
$LaSh_f$	LaSh	$\{(256, 128, 64, 24, 12, 6) \times (1.5, 0.75),\ 1/60\}$	0.4	-0.4	3.67

Table 2. Grid structure, evolution system *ES* and initial parameters of the simulations of quasi-circular inspirals. The grid setup is given in terms of the radii in units of M of the individual refinement levels as well as the resolution near the punctures h (see Sec. II E in [57] for details). In case of the LaSh scheme we also specify the densitization parameters n_Q and n_K. The final column lists the radiated energy $E_{\rm rad}$ extracted at $r_{\rm ex} = 60\ M$ for models $LaSh_c$-$LaSh_f$. Models $BSSN$ and $LaSh_0$ have only been run until $t = 50M$ in order to compare their computational cost.

Ref. [72]. This configuration represents a non-spinning, equal-mass binary with a total ADM mass of $M = 0.9957$ in code units. The bare-mass parameters are $m_{1,2} = 0.483$ and the BHs start at position $x_{1,2} = \pm 3.257$ with linear momentum $P_{1,2} = \pm 0.133$ in the y-direction. The specifications of the grid setup, in the notation of Sec. II E of Ref. [57], are given in Table 2. For this model we have used the Γ-driver shift condition 27 with $(\mu_s, \xi_1, \xi_2, \eta) = (3/4, 1, 1, 1)$ as suggested in Ref. [73]. As before, we study the convergence properties by performing simulations of model $LaSh$ with resolutions $h_c = 1/52$, $h_m = 1/56$ and $h_f = 1/60$. In the left panel of Fig. 7 we present the real part of the $\ell = 2$, $m = 2$ mode of Ψ_4, extracted at $r_{ex} = 40M$, obtained by models $LaSh_c$, $LaSh_m$ and $LaSh_c$. The right panel of Fig. 7 shows the differences between the coarse and medium and medium and high resolutions of the amplitude

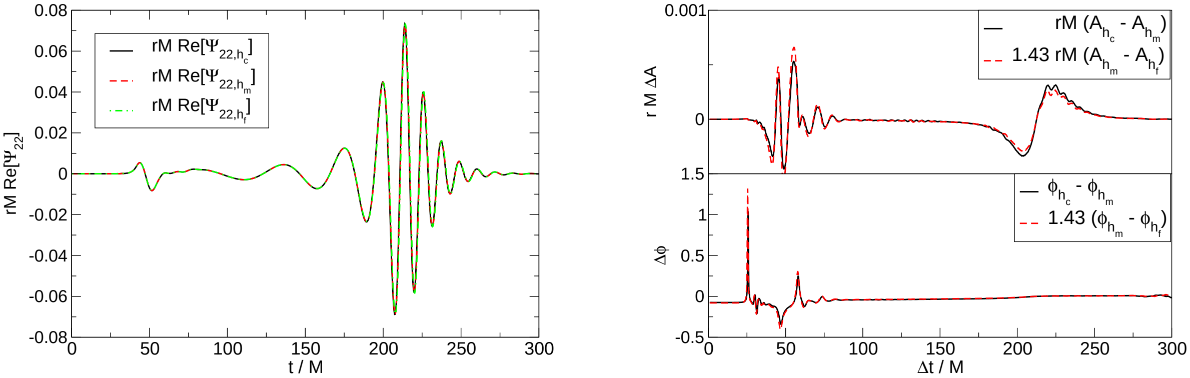

Figure 7. (Color online) Left: Real part of the dominant $\ell = 2$, $m = 2$ mode of the dimensionless Newman-Penrose scalar $rM\Re(\Psi_4)$, where the extraction radius is $r_{ex} = 40M$. The waveforms are shown for models $LaSh_c$ (black solid line), $LaSh_m$ (red dashed line) and $LaSh_f$ (green dash-dotted line). Right: Convergence analysis of the Amplitude (upper panel) and phase (bottom panel) of the dominant $\ell = 2$, $m = 2$ mode of the Newman Penrose scalar Ψ_4. We show the differences between the coarse and medium resolution (black solid line) and medium and high resolution (red dashed line). The latter difference has been amplified by $Q_4 = 1.43$, indicating fourth order convergence.

(upper panel) and phase (bottom panel). The latter differences have been rescaled by the factor $Q_4 = 1.43$ corresponding to fourth order convergence. The resulting discretization error in amplitude and phase are $\Delta A/A \leq 1\%$ and $\Delta\phi \leq 0.1$ rad.

The energy radiated in gravitational waves is $E_{rad}/M = 3.67 \pm 0.13\%$ for the high resolution run $LaSh_f$ in Table 2 which is in good agreement with the BSSN results of Ref. [57].

Run	mem. [GByte]	t_r [CPUhours]	$\bar{v}$ [M/hour]
$BSSN$	55	290	4.2
$LaSh_0$	70	430	2.9
$modLaSh$	55	335	3.7

Table 3. The required memory $mem.$, the total runtime t_r in CPUhours and the average speed $\bar{v}$ in units of physical time M per real time hour of the test simulations using the BSSN (model $BSSN$ in Table 2), the original LaSh (model $LaSh_0$ in Table 2) and the modified LaSh scheme. The simulations have been run for $t = 50M$ using 24 processors.

Finally, we compare the computational performance of both, the BSSN and LaSh evolution scheme. For this purpose we have evolved models $LaSh_0$ and $BSSN$ until $t = 50M$ on the Magerit cluster [74] in Madrid which is part of the Spanish Supercomputing Network [75]. Magerit uses PowerPC-970FC processors running at

$2.2GHz$. The required memory, runtime and average speed obtained for 24 processors are shown in Table 3. The original LaSh system requires about 30 % more memory than the BSSN system and is about a factor 1.4 slower. The overhead of the LaSh system is not unexpected. First, the LaSh system involves a larger number of grid functions; the tracefree part of the extrinsic curvature $\hat{A}^i{}_j$ is not symmetric and thus requires 9 independent components instead of 6 for the BSSN variable $\tilde{A}_{ij}$. Second, the densitization of variables requires extra variables and involved more complicated expressions on the right hand sides of the corresponding evolution equations. These effects can be partly eliminated, however, without loosing the appealing properties of the LaSh system. For this purpose, we have tested a modified version of the original LaSh system, denoted as *modLaSh* in Table 3. Here we evolve $\tilde{A}_{ij}$ instead of the trace-free part of the extrinsic curvature with mixed indices $\tilde{A}^i_j$. As expected, this modification equals the BSSN system in memory requirements and also significantly reduces the computational costs relative to the original LaSh system. At the same time, however, *modLaSh* preserves the flexibility that has enabled us to obtain smoother behaviour of the variables close to the puncture as compared with the BSSN scheme.

5. Conclusions

Motivated by a desire to better understand which are the important ingredients of the moving puncture method, we have studied the LaSh formulation of the Einstein equations. Provided that the algebraic constraints of the system are imposed the formulation is equivalent to BSSN. Therefore we have investigated how the choice of evolved variables effects the success of numerical simulations of puncture initial data. The change of variable is parametrized by the densitization parameters (n_Q, n_K).

We started by demonstrating that LaSh is formally numerically stable when linearized around flat space for arbitrary densitization parameters, with fixed shift and densitized lapse. A special case of this calculation is the numerical stability of BSSN. We attempted to show numerical stability of the system coupled to the puncture gauge, but find that the required calculations are too complicated even for computer algebra unless we move away from the standard discretization.

We performed four types of numerical tests. The first class of tests includes robust stability test, specifically the so-called apples with apples tests. We find that the LaSh formulation is numerically stable for various choices of the densitization parameters. Next, we found that long term stable evolutions of single BH spacetimes requires a more careful choice of the densitization parameters. It is interesting to note that the parameter choice corresponding to the BSSN system is located near the edge of the permissible range. Furthermore, we have identified parameter choices which result in smoother profiles of the time derivatives of the evolution variables near the puncture as compared with the BSSN case. It will be interesting to investigate the impact of this behaviour on the accuracy of inspiral simulations lasting $10 - 15$ orbits. While such a study is beyond the scope of this paper, it may provide fertile ground for direct application of the results presented in this work.

We have further evolved head-on collisions as well as quasi-circular inspirals of binary BHs. For both cases, we have achieved long-term stable evolutions for a wide range of non-trivial parameter choices (n_Q, n_K). The evolutions produce convergent waveforms consistent with the BSSN results and comparable accuracy. As mentioned above, we plan to compare the accuracy of both systems for more demanding inspiral simulations in future work. In any case, the binary simulations confirm the above finding that non vanishing values of n_Q and n_K facilitate evolutions with smoother profiles of the evolution variables in the neighborhood of each puncture.

In summary, our results highlight the importance of the choice of variables for numerical calculations aside from any continuum PDE considerations. This opens up the possibility of significantly reducing errors in simulations of astrophysical binaries with large spins or mass ratios and also overcome stability issues reported for higher dimensional BH simulations [49].

Acknowledgments

The authors are grateful to Emanuele Berti, Bernd Brügmann, Ian Hinder and Ronny Richter for helpful comments on the manuscript. H.W.'s work was partly supported by DFG grant SFB/ Transregio7 and by Fundação para a Ciência e Tecnologia (FCT) - Portugal through grant SFRH/BD/46061/2008 and through projects PTDC/FIS/098032/2008 and PTDC/FIS/098025/2008. D.H. was supported partly by DFG grant SFB/Transregio7. U.S. acknowledges support from the Ramón y Cajal Programme of the Spanish Ministry of Education and Science (MEC) as well as FCT – Portugal through project PTDC/FIS/098025/2008, the Sherman Fairchild Foundation to Caltech, by NSF grants PHY-0601459, PHY-0652995, PHY-1057238, by loni_numrel05, an allocation through the TeraGrid Advanced Support Program under grant PHY-090003 on NICS' kraken cluster and an allocation by the Centro de Supercomputación de Galicia (CESGA) under project ICTS-2009-40 on Finis Terae. This work was also supported by NSF Grant PHY-0900735 and by the *DyBHo–256667* ERC Starting Grant. Computations were partly performed at the LRZ Munich, Milipeia in Coimbra and Magerit in Madrid. The authors thankfully acknowledge the computer resources, technical expertise and assistance provided by the Barcelona Supercomputing Centre—Centro Nacional de Supercomputación.

References

[1] Jeffrey. E. McClintock and Ronald. A. Remillard. Black Hole Binaries. 2003.

[2] M.J. Rees. Black hole models for active galactic nuclei. *Ann. Rev. Astron. Astrophys.*, 22:471, 1984.

[3] Laura Ferrarese and Holland Ford. Supermassive Black Holes in Galactic Nuclei: Past, Present and Future Research. *Space Sci. Rev.*, 116:523–624, 2005.

[4] B. Abbott et al. Search for gravitational waves from binary black hole inspirals in LIGO data. *Phys. Rev.*, D73:062001, 2006.

[5] http://www.ligo.caltech.edu/.

[6] M. Hewitson. Detector and data characterization at GEO 600. *Class. Quant. Grav.*, 24:S445–S455, 2007.

[7] http://www.geo600.org/.

[8] F. Acernese et al. Virgo status. *Class. Quant. Grav.*, 25:184001, 2008.

[9] Masaki Ando et al. Stable operation of a 300-m laser interferometer with sufficient sensitivity to detect gravitational-wave events within our Galaxy. *Phys. Rev. Lett.*, 86:3950, 2001.

[10] K. Danzmann and A. Rudiger. LISA technology - Concept, status, prospects. *Class. Quant. Grav.*, 20:S1–S9, 2003.

[11] Luc Blanchet. Gravitational Radiation from Post-Newtonian Sources and Inspiralling Compact Binaries. *Living Rev. Rel.*, 4, 2006. http://www.livingreviews.org/Articles/lrr-2006-4/download/index.html, cited on 5 May 2009.

[12] Emanuele Berti, Vitor Cardoso, and Andrei O. Starinets. Quasinormal modes of black holes and black branes. *Class. Quant. Grav.*, 26:163001, 2009.

[13] Richard L. Arnowitt, Stanley Deser, and Charles W. Misner. The dynamics of general relativity. 1962.

[14] J. W. York, Jr. Kinematics and dynamics of general relativity. In L. L. Smarr, editor, *Sources of Gravitational Radiation*, pages 83–126, 1979.

[15] Frans Pretorius. Evolution of Binary Black Hole Spacetimes. *Phys. Rev. Lett.*, 95:121101, 2005.

[16] John G. Baker, Joan Centrella, Dae-Il Choi, Michael Koppitz, and James van Meter. Gravitational wave extraction from an inspiraling configuration of merging black holes. *Phys. Rev. Lett.*, 96:111102, 2006.

[17] Manuela Campanelli, C. O. Lousto, P. Marronetti, and Y. Zlochower. Accurate Evolutions of Orbiting Black-Hole Binaries Without Excision. *Phys. Rev. Lett.*, 96:111101, 2006.

[18] Frans Pretorius. Binary Black Hole Coalescence. 2007.

[19] Miguel Alcubierre. *Introduction to 3+1 numerical relativity* . International series of monographs on physics. Oxford Univ. Press, Oxford, 2008.

[20] Mark Hannam. Status of black-hole-binary simulations for gravitational- wave detection. *Class. Quant. Grav.*, 26:114001, 2009.

[21] Ian Hinder. The Current Status of Binary Black Hole Simulations in Numerical Relativity. *Class. Quant. Grav.*, 27:114004, 2010.

[22] Joan M. Centrella, John G. Baker, Bernard J. Kelly, and James R. van Meter. Black-hole binaries, gravitational waves, and numerical relativity. 2010.

[23] Sergio Dain, Carlos O. Lousto, and Yosef Zlochower. Extra-Large Remnant Recoil Velocities and Spins from Near- Extremal-Bowen-York-Spin Black-Hole Binaries. *Phys. Rev.*, D78:024039, 2008.

[24] Ulrich Sperhake, Vitor Cardoso, Frans Pretorius, Emanuele Berti, and Jose A. Gonzalez. The high-energy collision of two black holes. *Phys. Rev. Lett.*, 101:161101, 2008.

[25] Masaru Shibata, Hirotada Okawa, and Tetsuro Yamamoto. High-velocity collision of two black holes. *Phys. Rev.*, D78:101501, 2008.

[26] Ulrich Sperhake et al. Cross section, final spin and zoom-whirl behavior in high- energy black hole collisions. *Phys. Rev. Lett.*, 103:131102, 2009.

[27] Mark Hannam, Sascha Husa, Denis Pollney, Bernd Bruegmann, and Niall O'Murchadha. Geometry and Regularity of Moving Punctures. *Phys. Rev. Lett.*, 99:241102, 2007.

[28] J. David Brown. Puncture Evolution of Schwarzschild Black Holes. *Phys. Rev.*, D77:044018, 2008.

[29] J. David Brown. BSSN in Spherical Symmetry. *Class. Quant. Grav.*, 25:205004, 2008.

[30] Mark Hannam, Sascha Husa, Frank Ohme, Bernd Bruegmann, and Niall O'Murchadha. Wormholes and trumpets: the Schwarzschild spacetime for the moving-puncture generation. *Phys. Rev.*, D78:064020, 2008.

[31] Bernd Bruegmann. Schwarzschild black hole as moving puncture in isotropic coordinates. *Gen. Rel. Grav.*, 41:2131–2151, 2009.

[32] M. Shibata and T. Nakamura. Evolution of three-dimensional gravitational waves: Harmonic slicing case. *Phys. Rev.*, D52:5428–5444, 1995.

[33] Thomas W. Baumgarte and Stuart L. Shapiro. On the numerical integration of Einstein's field equations. *Phys. Rev.*, D59:024007, 1999.

[34] Pablo Laguna and Deirdre Shoemaker. Numerical stability of a new conformal-traceless 3+1 formulation of the Einstein equation. *Class. Quant. Grav.*, 19:3679–3686, 2002.

[35] Clifford M. Will. The confrontation between general relativity and experiment. *Living Rev. Rel.*, 9:3, 2005.

[36] Nicolas Yunes and Frans Pretorius. Dynamical Chern-Simons Modified Gravity I: Spinning Black Holes in the Slow-Rotation Approximation. *Phys. Rev.*, D79:084043, 2009.

[37] Marcelo Salgado, David Martinez-del Rio, Miguel Alcubierre, and Dario Nunez. Hyperbolicity of scalar-tensor theories of gravity. *Phys. Rev.*, D77:104010, 2008.

[38] Ignatios Antoniadis. A Possible new dimension at a few TeV. *Phys. Lett.*, B246:377–384, 1990.

[39] Nima Arkani-Hamed, Savas Dimopoulos, and G. R. Dvali. The hierarchy problem and new dimensions at a millimeter. *Phys. Lett.*, B429:263–272, 1998.

[40] Ignatios Antoniadis, Nima Arkani-Hamed, Savas Dimopoulos, and G. R. Dvali. New dimensions at a millimeter to a Fermi and superstrings at a TeV. *Phys. Lett.*, B436:257–263, 1998.

[41] Lisa Randall and Raman Sundrum. A large mass hierarchy from a small extra dimension. *Phys. Rev. Lett.*, 83:3370–3373, 1999.

[42] Lisa Randall and Raman Sundrum. An alternative to compactification. *Phys. Rev. Lett.*, 83:4690–4693, 1999.

[43] Juan Martin Maldacena. The large N limit of superconformal field theories and supergravity. *Adv. Theor. Math. Phys.*, 2:231–252, 1998.

[44] S. S. Gubser, Igor R. Klebanov, and Alexander M. Polyakov. Gauge theory correlators from non-critical string theory. *Phys. Lett.*, B428:105–114, 1998.

[45] Edward Witten. Anti-de Sitter space and holography. *Adv. Theor. Math. Phys.*, 2:253–291, 1998.

[46] Hirotaka Yoshino and Masaru Shibata. Higher-dimensional numerical relativity: Formulation and code tests. *Phys. Rev.*, D80:084025, 2009.

[47] Masaru Shibata and Hirotaka Yoshino. Nonaxisymmetric instability of rapidly rotating black hole in five dimensions. *Phys. Rev.*, D81:021501, 2010.

[48] Masaru Shibata and Hirotaka Yoshino. Bar-mode instability of rapidly spinning black hole in higher dimensions: Numerical simulation in general relativity. *Phys. Rev.*, D81:104035, 2010.

[49] Miguel Zilhao et al. Numerical relativity for D dimensional axially symmetric space-times: formalism and code tests. *Phys. Rev.*, D81:084052, 2010.

[50] Helvi Witek et al. Numerical relativity for D dimensional space-times: head- on collisions of black holes and gravitational wave extraction. *Phys. Rev.*, D82:10, 2010.

[51] Evgeny Sorkin and Matthew W. Choptuik. Generalized harmonic formulation in spherical symmetry. *Gen. Rel. Grav.*, 42:1239–1286, 2010.

[52] Evgeny Sorkin. An axisymmetric generalized harmonic evolution code. *Phys. Rev.*, D81:084062, 2010.

[53] Matthew W. Choptuik et al. Towards the final fate of an unstable black string. *Phys. Rev.*, D68:044001, 2003.

[54] Luis Lehner and Frans Pretorius. Black Strings, Low Viscosity Fluids, and Violation of Cosmic Censorship. *Phys. Rev. Lett.*, 105:101102, 2010.

[55] Kenneth A. Dennison, John P. Wendell, Thomas W. Baumgarte, and J. David Brown. Trumpet slices of the Schwarzschild-Tangherlini spacetime. 2010.

[56] Helvi Witek et al. Black holes in a box: towards the numerical evolution of black holes in AdS. 2010.

[57] Ulrich Sperhake. Binary black-hole evolutions of excision and puncture data. *Phys. Rev.*,

D76:104015, 2007.

[58] Horst R. Beyer and Olivier Sarbach. On the well posedness of the Baumgarte-Shapiro-Shibata-Nakamura formulation of Einstein's field equations. *Phys. Rev.*, D70:104004, 2004.

[59] Miguel Alcubierre et al. Gauge conditions for long-term numerical black hole evolutions without excision. *Phys. Rev.*, D67:084023, 2003.

[60] Gabriel Nagy, Omar E. Ortiz, and Oscar A. Reula. Strongly hyperbolic second order Einstein's evolution equations. *Phys. Rev.*, D70:044012, 2004.

[61] Carsten Gundlach and Jose M. Martin-Garcia. Well-posedness of formulations of the Einstein equations with dynamical lapse and shift conditions. *Phys. Rev.*, D74:024016, 2006.

[62] David Garfinkle, Carsten Gundlach, and David Hilditch. Comments on Bona-Masso type slicing conditions in long- term black hole evolutions. *Class. Quant. Grav.*, 25:075007, 2008.

[63] Sebastiano Bernuzzi and David Hilditch. Constraint violation in free evolution schemes: comparing BSSNOK with a conformal decomposition of Z4. *Phys. Rev.*, D81:084003, 2010.

[64] Gioel Calabrese, Ian Hinder, and Sascha Husa. Numerical stability for finite difference approximations of Einstein's equations. *J. Comput. Phys.*, 218:607–634, 2006.

[65] M. Chirvasa and S. Husa. Discretization of the Cauchy problem for second order in space, first order in time systems using high order finite difference operators. 2008.

[66] B. Gustafsson, H. O. Kreiss, and J. Oliger. *Time dependent problems and difference methods*. Wiley, 1995.

[67] Cactus Computational Toolkit. http://www.cactuscode.org/.

[68] Mesh refinement with Carpet. http://www.carpetcode.org/.

[69] Erik Schnetter, Scott H. Hawley, and Ian Hawke. Evolutions in 3D numerical relativity using fixed mesh refinement. *Class. Quant. Grav.*, 21:1465–1488, 2004.

[70] Marcus Ansorg, Bernd Bruegmann, and Wolfgang Tichy. A single-domain spectral method for black hole puncture data. *Phys. Rev.*, D70:064011, 2004.

[71] Miguel Alcubierre et al. Toward standard testbeds for numerical relativity. *Class. Quant. Grav.*, 21:589, 2004.

[72] John G. Baker, Joan Centrella, Dae-Il Choi, Michael Koppitz, and James van Meter. Binary black hole merger dynamics and waveforms. *Phys. Rev.*, D73:104002, 2006.

[73] Bernd Bruegmann et al. Calibration of Moving Puncture Simulations. *Phys. Rev.*, D77:024027, 2008.

[74] http://www.cesvima.upm.es/.

[75] http://www.bsc.es/.